Passive oscillations of inverted flags in a uniform flow

Yao-Wei Hu[1], Li-Hao Feng[1],† and Jin-Jun Wang[1]

[1]Fluid Mechanics Key Laboratory of Education Ministry, Beijing University of Aeronautics and Astronautics, Beijing 100191, China

The passive oscillations of inverted flags are investigated both experimentally and theoretically in this paper. First, the force and energy distributions of inverted flags, which contain elastic and inertia components, are analysed based on the experimental data. Two main differences between inverted and conventional flags are found: (1) the elastic energy of a conventional flag is concentrated near the free end, while the fixed end of an inverted flag presents the largest elastic energy; and (2) the elastic component is several orders of magnitude greater than the inertia component for an inverted flag, while they are of the same magnitude for a conventional flag. Second, a linear analysis shows that the critical flow velocities obtained from the experiments at small mass ratios are scattered around the theoretical curve of wavenumber $k = 1.875$, which is in contrast with $k = 4.694$ of a conventional flag. For large mass ratios, the mass ratio has a certain influence on the critical velocity rather than being irrelevant. For two parallel inverted flags, both the experimental and theoretical results indicate that the range of the in-phase flapping mode becomes smaller with an increase in the separation distance, and a multiple flapping state may occur. For $n \geqslant 2$ parallel inverted flags, the theoretical results show that two of all coupled flapping modes are dominant with most parameters. These findings could contribute to a better understanding of the passive oscillations of inverted flags.

Key words: aerodynamics, flow–structure interactions

1. Introduction

The oscillation of a flexible object in a uniform flow is a common phenomenon in nature. In previous studies, a flexible flag where one edge is fixed and the other edge is free, which is in fact a beam or thin plate whose primary stiffness is that of a beam or plate in elastic bending, has been proposed as a simplified model. A flag in the wind is called a conventional flag for its fixed leading edge and free trailing edge (Taneda 1968; Watanabe *et al.* 2002*a,b*; Jia *et al.* 2007; Shelley & Zhang 2011). In contrast, the leading edge of an inverted flag is free, and the trailing edge is fixed, e.g. flapping leaves in the wind (Kim *et al.* 2013; Sader *et al.* 2016).

In recent years, the hydrodynamic characteristics of flexible flags, including dynamical modes, shedding vortices and pressure jump, have attracted the attention of

† Email address for correspondence: lhfeng@buaa.edu.cn

researchers. For a conventional flag, Taneda (1968) first gave its two stable dynamical modes: straight and flapping modes. Zhang *et al.* (2000) creatively used a flowing soap film to study the trailing-edge vortices of the conventional flag. It was found that von Kármán-type vortices were shed from the fixed end in the straight mode. When the conventional flag entered the flapping mode, the successive small eddies produced by a single stroke were of a single sign, unlike the alternating signs in the stretched-straight mode. Kim *et al.* (2013) and Sader *et al.* (2016) further noted that the flapping of a conventional flag was due to flutter instability, indicating that the fluid force had a stabilizing effect for a conventional flag. Jia & Yin (2008) first described the force and energy distributions along two tandem conventional flags after obtaining their oscillation equations based on experiments. It was determined that the force and energy of the front flag were larger than those of the rear flag, which were even larger than those of a single conventional flag. For a deeper understanding of conventional flags, readers are referred to a review paper by Shelley & Zhang (2011).

Compared with a conventional flag, an inverted flag enters the unstable state at a lower critical velocity and with a larger amplitude (Kim *et al.* 2013). Therefore, an inverted flag is more valuable than a conventional flag in energy harvesting (Kim *et al.* 2013; Ryu *et al.* 2015; Tang, Liu & Lu 2015*a*; Tang, Gibbs & Dowell 2015*b*; Shoele & Mittal 2016; Orrego *et al.* 2017) and wall heat transfer (Park *et al.* 2016; Yu, Liu & Chen 2017, 2018; Chen *et al.* 2018). Kim *et al.* (2013) first studied the dynamic behaviours of an inverted flag. Three modes were found with a successive increase in the flow velocity: the straight mode, the large-amplitude flapping mode and the deflected mode. Gurugubelli & Jaiman (2015) further revealed the mechanism of entering the large-amplitude flapping mode and the reason for maintaining the oscillation through numerical simulations. Gurugubelli & Jaiman (2015) noted that the flapping instability was a static divergence instability, namely the fluid force caused the disturbance to continue to diverge for the inverted flag. After entering the large-amplitude flapping mode, the leading-edge vortex played an important role in maintaining the oscillation of the inverted flag. Hu *et al.* (2019) further confirmed the above conclusions in their experiments. The numerical results of Ryu *et al.* (2015) and Tang *et al.* (2015*a*) showed that the energy conversion ratio from the fluid kinetic energy to the strain energy of an inverted flag was as high as 0.4–0.6, indicating that the energy harvesting ability of an inverted flag was higher than that of a conventional flag, which was usually approximately 10^{-3}. Park *et al.* (2016) and Yu *et al.* (2017) recently applied an inverted flag to wall heat transfer and found that its periodical influence on the fluid near the wall enhanced the heat transfer effect. For two parallel inverted flags, five coupled flapping modes were observed by Huertas-Cerdeira, Fan & Gharib (2018), namely in-phase, anti-phase, staggered, alternating and decoupled flapping modes. In the case of small distances and low flow velocities, the anti-phase flapping mode was predominant. In addition, the in-phase flapping mode rarely occurred throughout the experiments.

Previous studies of inverted flags mainly adopted the methods of experiments and numerical simulations. However, theoretical analysis has been proven to be an effective tool for decomposing the displacement of a conventional flag in time and space (Allen & Smits 2001). Theoretical analyses might take less time than numerical simulations, but they have the same accuracy (Watanabe *et al.* 2002*b*). Shelley, Vandenberghe & Zhang (2005) mainly adopted a linear theoretical model, which ignored the finite length of the filament, the vortex shedding at the trailing edge and the effect of viscosity in order to obtain the critical velocities of a conventional flag. They found that this linear theoretical model gave a good estimate of the

critical speed at small mass ratios, while the prediction result was one order of magnitude lower at large mass ratios. They noted that the deviation was due to neglect of the viscous force, which was predominant at large mass ratios. Afterwards, Jia *et al.* (2007) applied the above theoretical model to two side-by-side conventional flags. They found that the flapping mode of two parallel conventional flags switched from the anti-phase mode to the in-phase mode with an increase in the flow velocity. Schouveiler & Eloy (2009) applied the theoretical model to three and four side-by-side conventional flags. They noted that the theoretical results agreed well with the experimental results, but the critical velocities between different flapping modes could not be well predicted. Based on the above theoretical model proposed by Shelley *et al.* (2005), Kim & Kim (2019) assumed $\omega = 0$ in order to obtain the critical velocities between the different coupled modes of two parallel inverted flags and studied the effect of the flag height-to-length ratio on the unstable boundary. In these studies, it was demonstrated that some intuitional results can be obtained readily using this linear theoretical model and that the coupling modes can be predicted qualitatively. Gibbs *et al.* (2014) and Tang *et al.* (2015*b*) further applied the vortex lattice method to consider vortex shedding from the trailing edge of a conventional flag and obtained theoretical results that are in good agreement with experimental results.

While the dynamic behaviours and flow fields of inverted flags have been studied, there is currently no in-depth study of the force and energy distributions along inverted flags. Therefore, we intend to experimentally study the force and energy distributions of an inverted flag in order to gain a deep understanding of their relationship with the flag oscillation. In addition, regardless of whether it is an inverted flag or a conventional flag, it maintains a straight path at a low flow velocity, and then enters a flapping mode as the flow velocity increases. To explore the physical mechanism of the mode transition, the critical velocities between the different flapping modes are theoretically studied using a simplified hydrodynamic model, which can be regarded as an extension of the single-flag model proposed by Shelley *et al.* (2005).

This article is organized as follows. Section 2 introduces the experimental set-up and theoretical model. Section 3 discusses the force and energy distributions, as well as theoretical analysis results. Finally, the main research results are summarized.

2. Experimental set-up and theoretical model

2.1. *Experimental method*

The experiments were conducted in the recirculating water tunnel of Beijing University of Aeronautics and Astronautics to obtain the deformed profiles of the inverted flag, as shown in figure 1. The test section of the water tunnel was 0.6 m wide and 0.7 m high. The flow velocity in this study ranged from 106 to 182 mm s^{-1}. The flag was made of polyvinyl chloride plastic with a density of $\rho_s = 1.3 \times 10^3$ kg m^{-3}. The flap was set at height $H = 140$ mm, length $L = 100$ mm and thickness $h = 0.24$ mm, which could ensure the two-dimensionality of the flag (Tang *et al.* 2015*a*; Hu *et al.* 2019). The trailing edge of the inverted flag was fixed by two semi-cylinders with a diameter of 4 mm. As presented in figure 1, the middle height position of the fixed end of the flag was set as the origin of the coordinates, the spanwise direction was defined as the y axis and the streamwise direction was defined as the x axis.

Referring to previous studies (Kim *et al.* 2013), the dimensionless flow velocity U_0^* and fluid-to-structure mass ratio M_S are two main dynamical parameters of the inverted
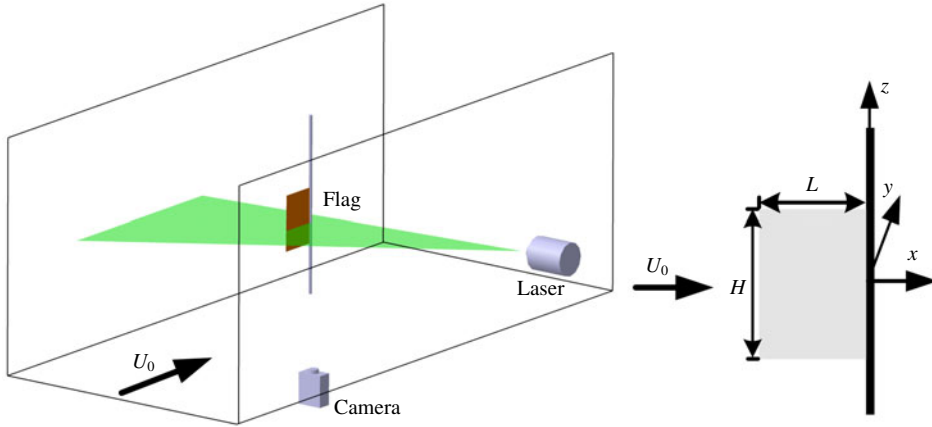
FIGURE 1. Schematic diagram of the experimental set-up.

flag, which are defined as follows:

$$U_0^* = U_0 L \sqrt{\frac{\rho_f L}{B}}, \tag{2.1}$$

$$M_S = \frac{\rho_f L}{\rho_S h}, \tag{2.2}$$

where the flexural rigidity of the flag is $B = Eh^3/[12(1 - \nu^2)]$, in which $E = 1173.3$ MPa is the Young's modulus. The density of the water is $\rho_f = 997$ kg m^{-3}. In this experiment, U_0^* was set as 2.52, 2.70, 2.88, 3.06, 3.24, 3.96 and 4.31; M_S was 320. Furthermore, as did Shelley *et al.* (2005), five steel sheets were attached on each surface of a special inverted flag at equal intervals to reduce its mass ratio and increase its inertial force. The height, width, thickness and density of the steel sheets were 100 mm, 4 mm, 0.2 mm and 7.8×10^3 kg m^{-3}, respectively. Similar to Shelley *et al.* (2005), we can also assume that the density and stiffness of the 'heavy' flag were uniform. Under this condition, M_S was reduced to 106.

The deformed profiles of the inverted flag at different moments were obtained by the boundary recognition algorithm, as given by Hu *et al.* (2019). The main implementation process of the boundary recognition algorithm was as follows. First, the original image was binarized. Then, the background noise in the binary image was filtered. Finally, the polynomial fitting method was used to obtain the deformed profiles of the inverted flag.

2.2. *Theoretical model*

The linear stability analysis of the two-dimensional inverted flag is described below. The theoretical analysis model of *n* parallel inverted flags is presented here, as shown in figure 2. The middle position of these *n* trailing edges is set as the origin of the coordinates, and the distance between every two adjacent inverted flags is *d*. Thus, the isolated inverted flag can be referred to as one typical case when *d* approaches infinity. For the directions of the *x* axis and *y* axis, refer to figure 1. The wall-normal displacements of the *n* inverted flags positioned at y_i are written as $\eta_i(x, t)$, where $i = 1, 2, \ldots n$. If the phase difference between two of the *n* flags is θ, then the two
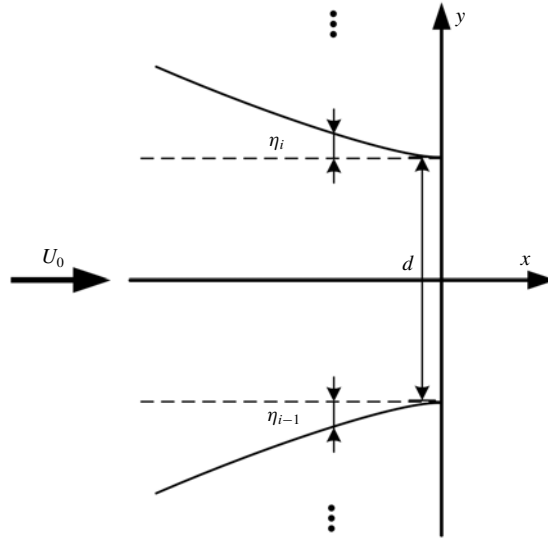
FIGURE 2. Theoretical model of n parallel inverted flags, where $i = 1, 2, \ldots n$.

flags oscillate in phase at $\theta = 0$ and oscillate out of phase at $\theta = \pi$. Hence, the critical flow velocity at which the n parallel inverted flags begin to oscillate, as well as the coupled flapping mode, can be obtained. According to the Euler–Bernoulli beam equation (Kornecki, Dowell & O'Brien 1976; Jia *et al.* 2007):

$$\rho_s h \partial_t^2 \eta_i + B \partial_x^4 \eta_i = \Delta p_i, \quad i = 1, 2, \ldots n, \tag{2.3}$$

where the subscripts $i = 1, 2, \ldots n$ indicate the n flags and $\Delta p_i = p_{i+1} - p_i$ is the pressure jump across the ith flag. The pressure p in the above equation can be obtained from the linear Bernoulli equation:

$$p_j = -\rho_f(\partial_t + U_0 \partial_x)\varphi_j, \quad j = 1, 2, \ldots (n+1), \tag{2.4}$$

where $j = 1, 2, \ldots (n+1)$ corresponds to $(n+1)$ regions divided by n inverted flags. Function $\Phi_j = \overline{\Phi}_j + \varphi_j$ is the velocity potential function of the above $(n+1)$ regions, which consists of the average $\overline{\Phi}_j$ and perturbation φ_j parts.

According to the linear instability analysis, φ_j can be written as

$$\varphi_j = \varphi_{0j}(y)\mathrm{e}^{\mathrm{i}(\omega t + kx)}, \quad j = 1, 2, \ldots (n+1), \tag{2.5}$$

where $\varphi_{0j}(y)$ is the amplitude of the initial perturbation, ω is the complex frequency and k is the wavenumber.

For an inviscid incompressible fluid, the perturbation velocity potential φ_j must satisfy the Laplace equation without considering the effects of temperature and gravity. Additionally, φ_j must satisfy the appropriate boundary conditions:

$$\begin{cases} \partial_y \varphi_i(x, y_i, t) = (\partial_t + U_0 \partial_x)\eta_i(x, t), \\ \partial_y \varphi_{i+1}(x, y_i, t) = (\partial_t + U_0 \partial_x)\eta_i(x, t), \end{cases} \quad i = 1, 2, \ldots n, \tag{2.6}$$

$$\Delta\varphi_j = 0, \quad j = 1, 2, \ldots (n+1). \tag{2.7}$$

Therefore, the wall-normal displacements $\eta_i(x, t)$ of the two inverted flags can also be written as

$$\eta_i(x, t) = \eta_{0i}\mathrm{e}^{\mathrm{i}(\omega t + kx)}, \quad i = 1, 2, \ldots n, \tag{2.8}$$

where η_{0i} is the initial amplitude of the inverted flag.

Substituting (2.5) and (2.8) into the boundary conditions (2.6) and Laplace equation (2.7), the perturbation velocity potential φ_j can be obtained. Afterwards, φ_j is substituted into the Euler–Bernoulli beam equation (2.3), and the following equations can be obtained:

$$A_{n\times n}\boldsymbol{\beta} = \begin{bmatrix} a_1 & a_2 & 0 & 0 & \cdots & 0 \\ a_2 & a_3 & a_2 & 0 & \cdots & 0 \\ 0 & a_2 & a_3 & a_2 & \cdots & 0 \\ \vdots & \vdots & \ddots & \ddots & \ddots & \vdots \\ 0 & 0 & \cdots & a_2 & a_3 & a_2 \\ 0 & 0 & \cdots & 0 & a_2 & a_1 \end{bmatrix} \begin{bmatrix} \eta_{01} \\ \vdots \\ \eta_{0n} \end{bmatrix} = 0, \tag{2.9}$$

$$\left.\begin{array}{c} a_1 = -\dfrac{\omega^2}{M_S} + U_0^{*-2}k^4 - \dfrac{1 + \coth(kd^*)}{k}(\omega + k)^2, \\[4mm] a_2 = \dfrac{\operatorname{csch}(kd^*)}{k}(\omega + k)^2, \\[4mm] a_3 = -\dfrac{\omega^2}{M_S} + U_0^{*-2}k^4 - \dfrac{2\coth(kd^*)}{k}(\omega + k)^2, \end{array}\right\} \tag{2.10}$$

where $d^* = d/L$.

On the basis of the solution identification theorem in linear equations, $|A_{n\times n}|$ must be equal to 0, that is

$$\begin{vmatrix} a_1 & a_2 & 0 & 0 & \cdots & 0 \\ a_2 & a_3 & a_2 & 0 & \cdots & 0 \\ 0 & a_2 & a_3 & a_2 & \cdots & 0 \\ \vdots & \vdots & \ddots & \ddots & \ddots & \vdots \\ 0 & 0 & \cdots & a_2 & a_3 & a_2 \\ 0 & 0 & \cdots & 0 & a_2 & a_1 \end{vmatrix} = 0. \tag{2.11}$$

The coupled flapping mode of every two parallel inverted flags depends on

$$\frac{\eta_{0l}}{\eta_{0m}} = G\mathrm{e}^{\mathrm{i}\theta_{lm}}, \quad l, m = 1, 2, \ldots n. \tag{2.12}$$

Here, G and θ_{lm} are the ratios of the amplitude and phase angle, respectively. When $\theta_{lm} = 0$ or π, the two inverted flags are in the in-phase or anti-phase flapping modes, respectively.

3. Results and discussion

In this article we mainly focus on the oscillation of inverted flags. Since inverted flags are used to collect energy, it is critical to study the force and energy distributions of the inverted flags. Considering that the magnitude of the force and energy is
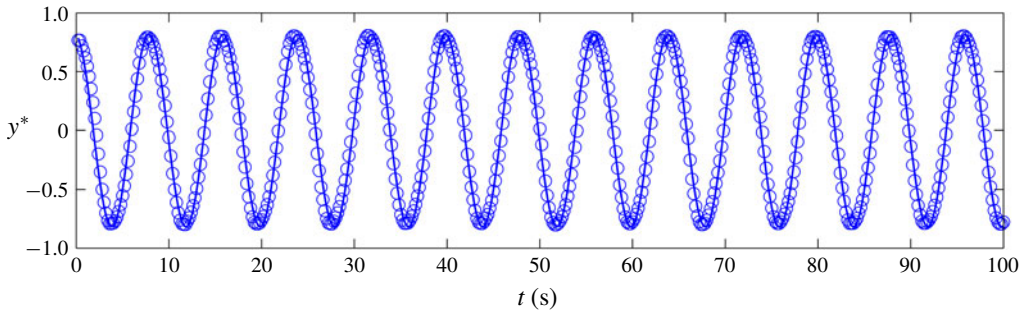
FIGURE 3. Variation of the tip spanwise displacement at $U_0^* = 2.88$, where the circles and the curve represent the experimental and fitting results, respectively.

closely related to the flapping mode, it is of great significance to determine the critical velocities between different modes via theoretical analysis. Therefore, the force and energy distributions of the inverted flag are studied first, followed by a theoretical prediction of the critical velocities. We verify the applicability of the theoretical model through the experimental results for both one flag and two flags and finally extend it to n flags.

3.1. *Force and energy distributions*

Taking $U_0^* = 2.88$ as an example, figure 3 shows the periodic oscillation of the free end over time based on the experimental data, where the circles and curve correspond to the experimental and fitting results, respectively. The equation of this curve is $y(t) = 0.8L \sin(2\pi \times 0.13t + \varphi_0)$, where $0.8L$ is the amplitude, 0.13 is the flapping frequency and φ_0 is the initial phase at $t = 0$. The other positions along the inverted flag also have similar fitting results, and there is no phase difference between the different positions. When the initial phase $\varphi_0 = 0$, the spanwise oscillation of the inverted flag can be approximately described as

$$y(s, t) = A(s) \sin(2\pi f_\omega t), \tag{3.1}$$

where s is the curve coordinate from the fixed end to the free end, $A(s)$ is the amplitude at different positions and f_ω is the flapping frequency.

For $U_0^* = 2.88$, $A(s) = -1.2162 \times 10^3 s^5 + 722.5 s^4 - 153.4 s^3 + 15.53 s^2 + 0.17s$. Then, the spanwise oscillation of the inverted flag can be described as

$$y(s, t) = (-1.2162 \times 10^3 s^5 + 722.5 s^4 - 153.4 s^3 + 15.53 s^2 + 0.17s) \sin(2\pi \times 0.13t). \tag{3.2}$$

In addition, the streamwise oscillation of the inverted flag can be obtained by $(\partial x / \partial s)^2 + (\partial y / \partial s)^2 = 1$.

A comparison of the fitting and experimental results is shown in figure 4. Figures 4(a) and 4(b) present the spanwise displacement at each point and the dynamic profiles of the inverted flag, respectively, where $s^* = s/L$, $x^* = x/L$ and $y^* = y/L$. The left-hand panel of each pair shows the fitting results, and the right-hand panel the experimental results. The results obtained by the above method are in good agreement with the experimental results.

After obtaining the oscillation equation of the inverted flag, the force and energy distributions at different times can be further statistically analysed. Referring to Jia &
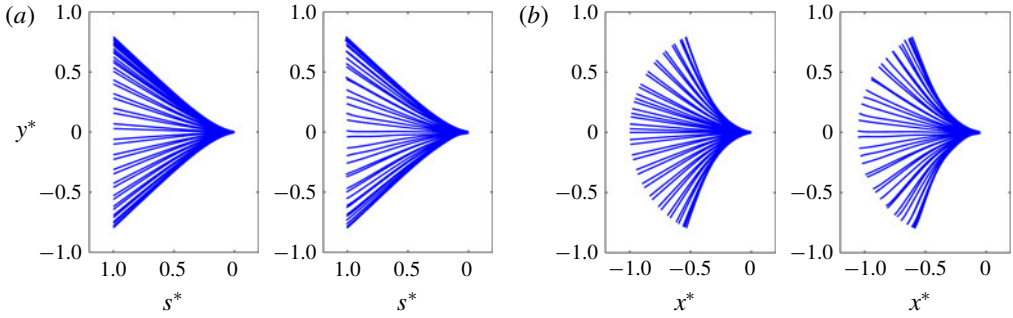
FIGURE 4. A comparison of the fitting and experimental results of the flag profiles at $U_0^* = 2.88$: (*a*) spanwise displacement at each point along the inverted flag; (*b*) dynamic profiles of the inverted flag. The left-hand and right-hand panels of each pair represent the fitting and experimental results, respectively.

Yin (2008), the equations for the force and energy distributions of a two-dimensional flag are as follows:

$$\left.\begin{aligned}
f_1 &= B\frac{\partial^4 y}{\partial s^4}, \\
f_2 &= \rho_s h\frac{\partial^2 y}{\partial t^2}, \\
f_y &= f_1 + f_2,
\end{aligned}\right\} \tag{3.3}$$

$$\left.\begin{aligned}
e_p(s,t) &= \frac{B}{2}\frac{(\partial^2 y/\partial s^2)^2}{1 - (\partial y/\partial s)^2}, \\
e_k(s,t) &= \frac{\rho_s h}{2}\left[\left(\frac{\partial x}{\partial t}\right)^2 + \left(\frac{\partial y}{\partial t}\right)^2\right], \\
e(s,t) &= e_p(s,t) + e_k(s,t).
\end{aligned}\right\} \tag{3.4}$$

Here, f_1, f_1 and f_y are the elastic force, inertia force and total distributed force in the y direction, respectively; and e_p, e_k and e are the strain energy, kinetic energy and total distributed energy, respectively.

The force and energy distributions for a representative case of $U_0^* = 2.88$ are given below. Figure 5 shows the variation of the force distribution and the tip displacement over a period. Figure 5(*a*) presents the distribution of the elastic force f_1 in one cycle, corresponding to the force that causes the flag to be bent. It can be determined that the elastic force f_1 reaches a maximum at the fixed end ($s^* = 0$) of the inverted flag, gradually decreases along the flag and is mainly concentrated in the range $0 \leqslant s^* \leqslant 0.5$. Thus, the bending of the inverted flag is mainly concentrated near the fixed end. Since the elastic force f_1 causes the flag to bend, the elastic force f_1 at different positions and the tip displacement present the same trend over time. During the periods 0–0.25T and 0.5T–0.75T, the inverted flag is in the bending process. The larger the displacement of the flag, the larger the elastic force f_1. During the periods 0.25T–0.5T and 0.75T–T, the inverted flag is in the rebounding process. The displacement and elastic force f_1 then gradually decrease. The above results show that the elastic force f_1 reaches a minimum at the equilibrium position (i.e. $t/T = 0, 0.5, 1$) and a maximum at the leftmost or rightmost position (i.e. $t/T = 0.25, 0.75$).
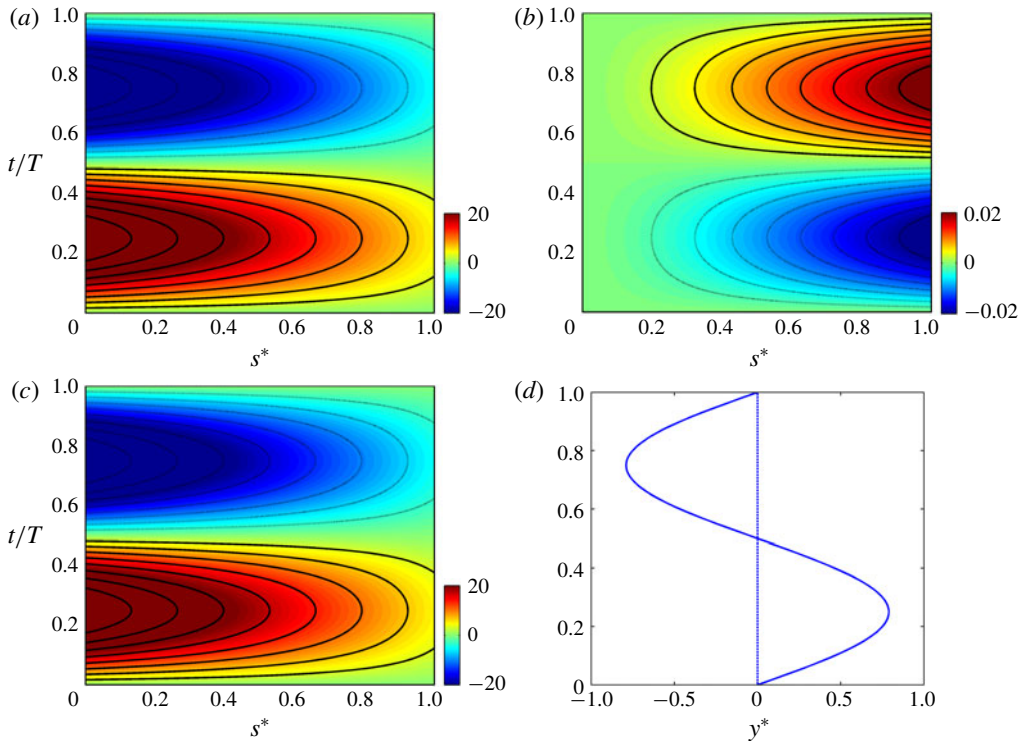
FIGURE 5. Variation of the force distribution in a period: (*a*) the elastic force f_1 (N m^{-1}), (*b*) the inertia force f_2 (N m^{-1}) and (*c*) the distributed force $f_y = f_1 + f_2$ (N m^{-1}). (*d*) Variation of the tip displacement in a period.

Figure 5(*b*) displays the distribution of the inertia force f_2 in one cycle, corresponding to the force that causes the flag to oscillate. In contrast to the elastic force f_1, the inertia force f_2 gradually increases along the flag and is the largest at the free end ($s^* = 1$) of the inverted flag. This phenomenon is mainly because the acceleration of the flag can be calculated from the oscillation equation (3.1) as $-4\pi^2 f_\omega^2 A(s) \sin(2\pi f_\omega t)$, resulting in the maximum acceleration at the free end of the inverted flag. It also causes an opposite trend of the inertia force f_2 and the tip displacement.

By comparing figures 5(*a*) and 5(*b*), it can be determined that the elastic force f_1 is approximately 10^3 times the inertia force f_2. Although the trends of these two types of forces are opposite over time, the trends and magnitudes of the distributed force f_y are almost the same as those of the elastic force f_1, as shown in figure 5(*c*). This is explainable because the distributed force f_y of the inverted flag is mainly completely provided by the elastic force f_1 during the oscillation process.

Figure 6 shows the variation of the energy distribution and the tip displacement over a period. Figures 6(*a*) and 6(*b*) present the distributions of the strain energy e_p and the kinetic energy e_k, respectively. Figure 6(*c*) gives the energy distribution $e = e_p + e_k$ in one cycle. From figures 5(*a*) and 6(*a*), it is determined that the trend of the strain energy e_p along the flag is the same as that of the elastic force f_1, both of which gradually decrease along the flag due to the maximum degree of bending of the fixed end. According to the expression of e_p in (3.4), the strain energy e_p at different
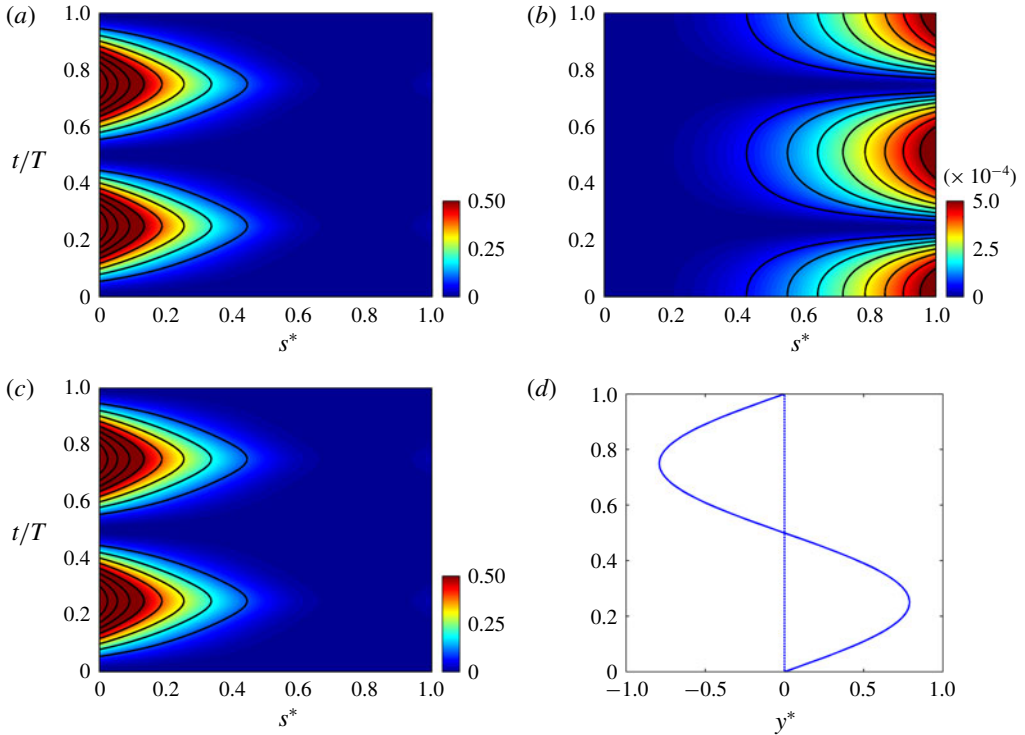
FIGURE 6. Variation in the energy distribution in a period: (*a*) the strain energy e_p (J m^{-1}), (*b*) the kinetic energy e_k (J m^{-1}) and (*c*) the distributed energy $e = e_p + e_k$ (J m^{-1}). (*d*) Variation of the displacement of the tip in a period.

positions and the absolute value of the tip displacement show the same trend over time. Given that the velocity of the flag can be written as $2\pi f_\omega A(s)\cos(2\pi f_\omega t)$, the kinetic energy e_k gradually decreases along the flag, and a phase difference of $0.25T$ occurs between it and the absolute value of the tip displacement (see figure 6*b*,*d*). Similar to that shown in figure 5, the strain energy e_p is also approximately 10^3 times the kinetic energy e_k. Thus, the trends of the distributed energy e and the strain energy e_p are almost identical.

Both figures 5 and 6 show that the elastic component (i.e. f_1 and e_p) is several orders of magnitude greater than the inertia component (i.e. f_2 and e_k). In contrast, these two components of a conventional flag are of the same magnitude (Jia 2009). This is mainly because the flag stiffness required for the large-amplitude flapping of the inverted flag is several orders of magnitude larger than that of the conventional flag under the same conditions. Additionally, the elastic component of the conventional flag is concentrated near the free end because its tip bends the most (Jia 2009), which is contrary to the results for the inverted flag in our study.

The force and energy distributions in figures 5 and 6 are integrated along the flag, and then the variation in the total force and total energy in one cycle can be obtained. Figures 7(*a*) and 7(*b*) give the time history of the total force F_y in the y direction and the total energy E in one cycle, respectively. As shown in figures 5(*c*) and 7(*a*), the trend of F_y is similar to that of the distributed force f_y. This phenomenon is mainly because the distributed force f_y has the same trend at different positions (see
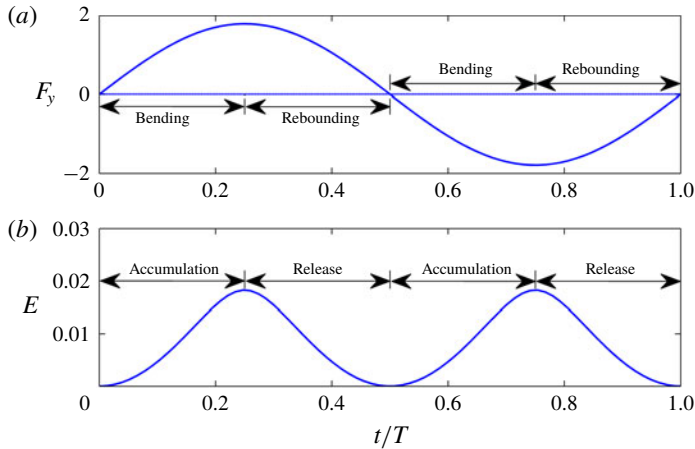
FIGURE 7. Variation of (*a*) the total force F_y (N) in the *y* direction and (*b*) the total energy *E* (J) in a period.

figure 5*c*). Specifically, F_y of the inverted flag is constantly increasing during the bending process, and in the rebound process F_y decreases continuously. As depicted in figures 6(*c*) and 7(*b*), the trends of the total energy *E* and the distributed energy *e* are also identical. The total energy *E* continues to increase during the bending process, corresponding to the energy accumulation process. In other words, the inverted flag collects energy from the surrounding fluid in the bending process. Additionally, the trend of the total energy *E* is opposite in the rebounding process, corresponding to the energy release process. Under this condition, the inverted flag releases energy into the surrounding fluid through the leading-edge vortex.

The time-averaged energy $\overline{E} = (1/T) \int_0^T E \, dt$ of the inverted flag can be further evaluated. The conversion ratio, defined as $R = E_{max}/E_f$ (Kim *et al.* 2013; Ryu *et al.* 2015), represents the efficiency of energy harvesting from the fluid kinetic energy to the flag strain energy; $E_f = 0.5\rho_f U_0^3 A$ is the kinetic energy of the uniform flow in which E_{max} the strain energy at the maximum deformation position, and *A* is the amplitude of the inverted flag. Figure 8 shows the time-averaged energy $\overline{E}$, the amplitude *A* and the conversion ratio *R* at different flow velocities. In addition, the critical velocities between the straight, flapping and deflected modes are marked by dashed lines. For the definition of these three modes, see Hu *et al.* (2019). It is determined from figure 8(*a*) that the trend of the time-averaged energy $\overline{E}$ is essentially consistent with that of the amplitude *A/L* as a function of the flow velocity, indicating that the amplitude of the inverted flag gives a good estimate of the strain energy. The present results further reveal that the averaged energy $\overline{E}$ in the deflected mode is equivalent to that in the flapping mode. As shown in figure 8(*b*), the conversion ratio *R* first increases and then decreases with the successive increase in the flow velocity. The maximum conversion ratio *R* immediately follows the critical velocity, which is earlier than for the experimental results of Kim *et al.* (2013) in a wind tunnel. Unlike the averaged energy $\overline{E}$ plotted in figure 8(*a*), the conversion ratio *R* of the deflected mode is far lower than that of the flapping mode.
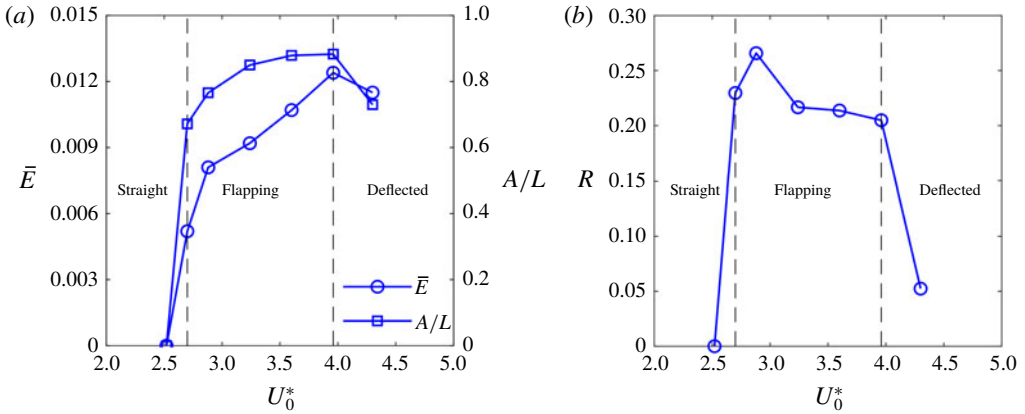
FIGURE 8. Variation in (*a*) the average energy $\overline{E}$ and amplitude A/L and (*b*) conversion ratio R at different flow velocities.

3.2. *Linear analysis*

The force and energy distributions of an isolated inverted flag during the oscillation process are analysed above. It can be concluded that the averaged energy and conversion ratio are considerable in the flapping mode. Hence, it is of great significance to determine the critical velocities between the different modes. To achieve this goal, a theoretical analysis provides us with a more convenient but sufficiently accurate approach in comparison with the experimental means. Thus, a theoretical analysis is further conducted to reveal the characteristics of the critical velocities. To give a global overview, isolated and multiple inverted flags will be analysed.

For the linear stability analysis of an isolated inverted flag ($n = 1$), equation (2.11) can be written as

$$(\omega + k)^2 + \left(\frac{k\omega^2}{M_S} - U_0^{*-2}k^5 \right) \bigg/ 2 = 0. \tag{3.5}$$

The imaginary part $\pm\omega_i$ of the complex frequency ω corresponds to the growth rate of disturbance. When $\omega_i > 0$ the inverted flag is unstable. To investigate the effect of M_S and U_0^* on the dynamic behaviour of the inverted flag, the wavenumber k must first be determined. For a cantilever beam with one end fixed and one end free, the wavenumbers of the first three modes are $k = 1.875$, 4.694 and 7.855, respectively (Young & Felgar 1949). Substituting the wavenumbers of the first three modes into (3.5), the critical flow velocities can be obtained (see the curves in figure 9). The critical flow velocities obtained from previous experiments (Kim *et al.* 2013; Fan 2015; Sader *et al.* 2016) and theoretical results (based on Kim & Kim (2019)) are also shown in figure 9. It can be determined that the critical flow velocities obtained from the experiments are located around the theoretical curve of wavenumber $k = 1.875$, especially at a small mass ratio. This is mainly because the value of ω in (3.5) is indeed almost zero for a small mass ratio, which is similar to the result of assuming $\omega = 0$ by Kim & Kim (2019). This further explains the applicability of the above theoretical model for a small mass ratio. For an isolated conventional flag, however, the critical flow velocity corresponds to the wavenumber
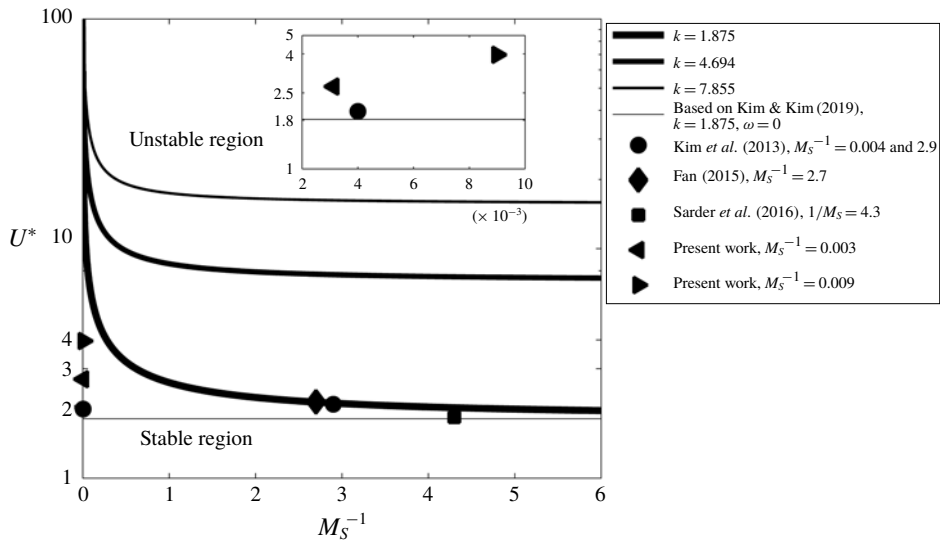
FIGURE 9. The curves represent the critical flow velocities of an isolated inverted flag at different wavenumbers k, and the symbols represent the results of previous experiments.

of the second mode $k = 4.694$ (Schouveiler & Eloy 2009). Thus, although there is a great difference between inverted and conventional flags, the applicability of this theoretical model to an isolated inverted flag is acceptable.

However, figure 9 also shows that for large mass ratios, the critical velocity obtained in our experiment is much larger than that of the theoretical results of Kim & Kim (2019). Additionally, the discrepancy between our experimental and theoretical results can reach an order of magnitude. Specifically, the critical velocity obtained in our experiment is $U_0^* = 2.7$; in contrast, the result predicted by the theoretical model is 33.6, and the result based on Kim & Kim (2019) is 1.815. The reasons for the discrepancies are as follows. The experiments in previous studies (Kim *et al.* 2013; Yu *et al.* 2017, 2018; Chen *et al.* 2018) using a water tunnel yielded a single-side small-amplitude flapping mode (i.e. a biased mode). When $\omega = 0$ is assumed, the critical velocity obtained in the above condition is the critical velocity at which the biased mode, rather than the large-amplitude flapping mode, begins to occur. Without assuming $\omega = 0$, the static divergence instability is not satisfied, resulting in an excessive prediction result. Additionally, the same degree of discrepancy was also found by Shelley *et al.* (2005) for a conventional flag at large mass ratios due to the ignoring of the viscous force in (2.3). The viscous force has a diverging effect for the inverted flag, thus leading to a larger prediction result (see figure 9). In contrast, the viscous force causes the conventional flag to be stable, and thus a smaller prediction result was found (Shelley *et al.* 2005). To reduce the effect of the viscous force and improve the reliability of (2.3), an additional experiment was performed on a special inverted flag with five steel sheets attached on each surface; thus, the mass ratio is reduced to $M_S = 106$. The results show that the critical velocity is then increased to 3.96, which is significantly improved compared to the critical velocity of 2.7, and becomes closer to the results of the theoretical prediction. However, the critical velocity at which a large-amplitude oscillation disappears does not change. This indicates that the mass ratio has a certain impact on the critical velocity for the water tunnel experiments.

In conclusion, although the oscillation of the inverted flag is caused by static divergent instability, the mass ratio can affect the critical velocity to some extent in a water tunnel, and ω is almost zero in a wind tunnel. Therefore, unlike Kim & Kim (2019), while we do not directly assume $\omega = 0$, the above results are highly reliable. As shown below, the theoretical model is mainly applied to inverted flags at small mass ratios.

To further verify the practicality of the theoretical model for inverted flags at small mass ratios, we compare the theoretical and experimental results for two parallel inverted flags. For the linear stability analysis of two inverted flags ($n = 2$), four solutions of the complex frequency ω in (2.11) can be obtained for determined d^*, M_S and U_0^*. The imaginary parts ω_{1i} obtained by $a_1 - a_2 = 0$ indicate that the two inverted flags are in the anti-phase flapping mode since $G = 1$ and $\theta_{12} = \pi$ (see (2.12)). Similarly, the imaginary part ω_{2i} obtained by $a_1 + a_2 = 0$ indicates that the two inverted flags are in the in-phase flapping mode since $G = 1$ and $\theta_{12} = 0$ (see (2.12)). When $\omega_{1i} > 0$ or $\omega_{2i} > 0$, the two inverted flags begin to oscillate. The coupled flapping mode depends on the relative sizes of ω_{1i} and ω_{2i}. Therefore, the definition of the disturbance growth rate ratio γ is as follows:

$$\gamma = \frac{\omega_{2i}}{\omega_{1i}}. \tag{3.6}$$

Figure 10 shows the statistical analysis of the disturbance growth rate ratio γ in the (M_S, U_0^*)-plane under different separation distances. The $\gamma < 1$ region corresponds to the anti-phase flapping mode (region II). The $\gamma > 1$ region corresponds to the in-phase flapping mode (region III). The $\gamma = 1$ region corresponds to the indefinite flapping mode (region IV), in which the coupled flapping mode cannot be determined. The solid line corresponds to the critical flow velocity where the two parallel inverted flags convert between different modes. As shown in figure 10, two inverted flags are both in the straight mode (region I) at a low flow velocity. As the flow velocity increases, the two inverted flags enter the anti-phase flapping mode and finally enter the in-phase flapping mode, which is consistent with the experimental results in a wind tunnel (Huertas-Cerdeira *et al.* 2018). When $d^* \approx 0$, the two inverted flags can be regarded as one inverted flag. In this case, the two inverted flags always oscillate in phase (see figure 10a). As presented in figure 10(b–d), region III (the in-phase flapping mode) becomes smaller, and the disturbance growth rate ratio γ in region II becomes closer to 1. When $d^* = 4$, the indefinite flapping mode (region IV) occurs. Additionally, the disturbance growth rate ratio γ is almost always 1 in region II or, to be exact, always larger than 0.999. Given the uncertainties in the experiments, the two inverted flags may enter a multiple flapping state dominated by the anti-phase flapping mode under this condition.

Figure 11 presents the results of the theoretical analysis for two inverted flags with different disturbances but a fixed mass ratio of 0.42, with the experimental results of the in-phase and anti-phase flapping modes from the previous experiment of Huertas-Cerdeira *et al.* (2018) also being given. The thin solid curve in region II represents $\gamma = 0.99$. The theoretical analysis shows that the in-phase flapping mode (region III) only occurs at small separation distances. With an increase in the flap distance, the in-phase flapping mode disappears, and the anti-phase flapping mode (region II) occurs. In general, the present predicted critical velocities for the anti-phase flapping mode are quite close to the experimental data. In region II, the disturbance growth rate ratio γ first decreases rapidly before gradually increasing. When $d^* > 2$, the disturbance growth rate ratio γ begins to be greater than 0.99, which is denoted as the region to
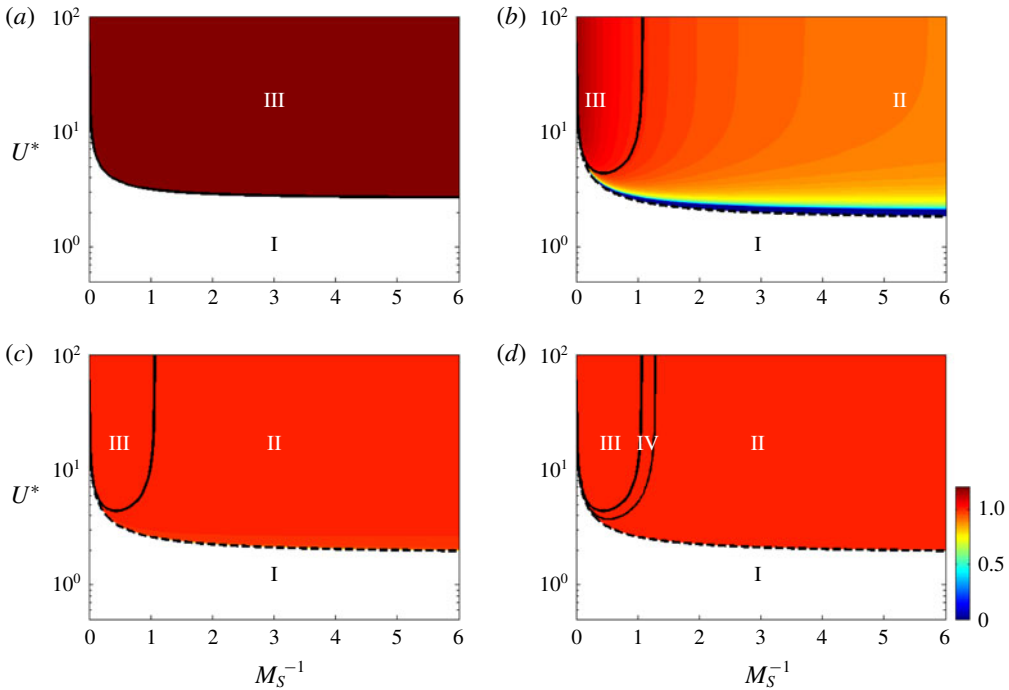
FIGURE 10. Contour plot denoting the disturbance growth rate ratio γ in the (M_S, U_0^*)-plane under different separation distances: (*a*) $d^* = 0.0001$, (*b*) $d^* = 1$, (*c*) $d^* = 2$ and (*d*) $d^* = 4$. Region I corresponds to the straight mode (γ is not a number); II corresponds to the anti-phase flapping mode ($\gamma < 1$); III corresponds to the in-phase flapping mode ($\gamma > 1$); and IV corresponds to the indefinite mode ($\gamma = 1$).

the right of the thin solid curve. Under this condition, the perturbation growth rates of the in-phase and anti-phase flapping modes are almost the same, and the two inverted flags may enter a multiple flapping state. Therefore, the critical velocities obtained from the experiment in which the anti-phase oscillation begins to disappear are located near $\gamma = 0.99$. It can be concluded that the inviscid model presents a good estimate of the critical velocities between the different flapping modes and explains the occurrence of multiple flapping states at a mass ratio of approximately 1, fully indicating the good applicability, easy operability and high reliability of the theoretical model for two parallel inverted flags.

Since the results of the theoretical model are in good agreement with the experimental results of a single and two inverted flags at small mass ratios, it can be concluded that this model has a certain practicability for studying the oscillation of inverted flags at small mass ratios. Then, we extend two flags to $n > 2$ flags in order to study the coupled flapping modes of multiple inverted flags. For $n > 2$ inverted flags, the method of determining the coupled flapping mode is similar to that for the two inverted flags (see (2.11) and (2.12)). Figure 12 shows the critical velocities at which the different flapping modes begin to occur in the (M_S, U_0^*)-plane for $n = 3$ and 4 and $d^* = 2$. When $n = 3$, three flapping modes are predicted by the theoretical model: $\eta_{01}/\eta_{03} = 1$, $\eta_{02}/\eta_{03} = -p_{31}$ (mode 1); $\eta_{01}/\eta_{03} = 1$, $\eta_{02}/\eta_{03} = p_{32}$ (mode 2); and $\eta_{01}/\eta_{03} = -1$, $\eta_{02} = 0$ (mode 3). Here p_{31} and p_{32} are two positive coefficients that are only related to M_S and U_0^*. When $n = 4$, four flapping modes are predicted by the
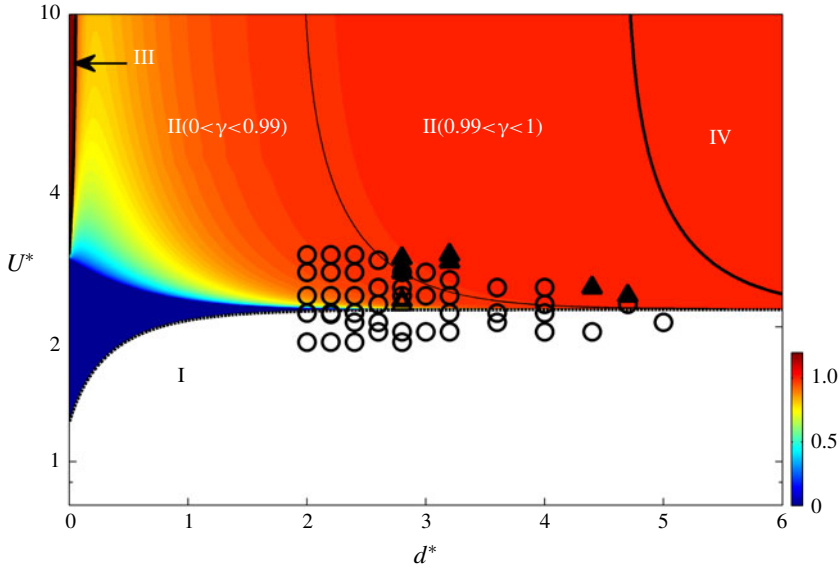
FIGURE 11. Contour plot denoting the disturbance growth rate ratio γ in the (d^*, U_0^*)-plane at $M_S = 0.42$. The definitions of regions I, II, III and IV are presented in figure 10. Symbols ▲ (in-phase) and ○ (anti-phase) represent the experimental results in a wind tunnel ($M_S = 0.42$) conducted by Huertas-Cerdeira *et al.* (2018).
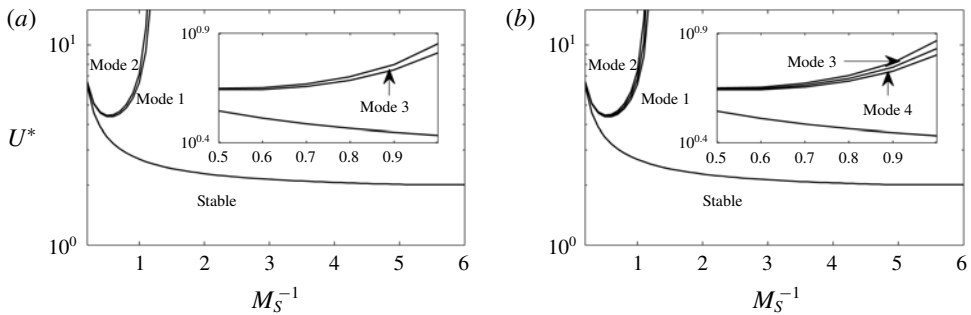

FIGURE 12. (*a*) Observation of the coupled flapping modes of $n = 3$ and $d^* = 2$: $\eta_{01}/\eta_{03} = 1$, $\eta_{02}/\eta_{03} = -p_{31}$ (mode 1); $\eta_{01}/\eta_{03} = 1$, $\eta_{02}/\eta_{03} = p_{32}$ (mode 2); and $\eta_{01}/\eta_{03} = -1$, $\eta_{02} = 0$ (mode 3). (*b*) Observation of the coupled flapping modes of $n = 4$ and $d^* = 2$: $\eta_{01}/\eta_{04} = -1$, $\eta_{02}/\eta_{03} = -1$, $\eta_{01}/\eta_{02} = -p_{41}$ (mode 1); $\eta_{01}/\eta_{04} = 1$, $\eta_{02}/\eta_{03} = 1$, $\eta_{01}/\eta_{02} = p_{42}$ (mode 2); $\eta_{01}/\eta_{04} = -1$, $\eta_{02}/\eta_{03} = -1$, $\eta_{01}/\eta_{02} = p_{43}$ (mode 3); and $\eta_{01}/\eta_{04} = 1$, $\eta_{02}/\eta_{03} = 1$, $\eta_{01}/\eta_{02} = -p_{44}$ (mode 4).

theoretical model: $\eta_{01}/\eta_{04} = -1$, $\eta_{02}/\eta_{03} = -1$, $\eta_{01}/\eta_{02} = -p_{41}$ (mode 1); $\eta_{01}/\eta_{04} = 1$, $\eta_{02}/\eta_{03} = 1$, $\eta_{01}/\eta_{02} = p_{42}$ (mode 2); $\eta_{01}/\eta_{04} = -1$, $\eta_{02}/\eta_{03} = -1$, $\eta_{01}/\eta_{02} = p_{43}$ (mode 3); and $\eta_{01}/\eta_{04} = 1$, $\eta_{02}/\eta_{03} = 1$, $\eta_{01}/\eta_{02} = -p_{44}$ (mode 4). Here p_{41}, p_{42}, p_{43} and p_{44} are four positive coefficients related to M_S and U_0^*. It can be determined that only two kinds of flapping modes are observed under most parameters at $n = 3$ and 4. Additionally, several other flapping modes are concentrated in only a small parameter range. Similarly, for $n = 5$, 6 and 7 inverted flags, the theoretical model predicts 6, 8

and 12 coupled flapping modes, respectively. By analogy, when $n = 2q$ $(q \geqslant 1)$, the theoretical model predicts 2^q coupled flapping modes; when $n = 2q + 1$, $2^q + 2^{(q-1)}$ coupled flapping modes are predicted by the theoretical model.

4. Concluding remarks

In this article, the force and energy distributions and the linearization analysis of an inverted flag are studied. First, the oscillation equation of the inverted flag is obtained. Subsequently, the relationship between the force and energy distributions and the oscillation of the flag is analysed. The applicable conditions of the inviscid model and the theoretical analysis results of n parallel inverted flags are also presented. The main conclusions are as follows.

The force and energy analysis indicates that there are two significant differences between conventional and inverted flags. First, the analysis of the force and energy distributions shows that the distributed force and energy are almost completely provided by the elastic component for the inverted flag, while the elastic and inertia components make the same contribution to the distributed force and energy for the conventional flag. This is because the flapping inverted flag requires a stiffness that is several orders of magnitude greater than a conventional flag under the same conditions. Second, due to the maximum bending at the fixed end, the distributed force and energy of the inverted flag are both mainly concentrated there. In contrast, the free end of the conventional flag bends the most and presents the largest distributed force and energy.

As far as the entire inverted flag is concerned, it obtains energy from the surrounding fluid in the bending process. In the rebounding process, its energy is released into the surrounding fluid through the leading-edge vortex. Additionally, the time-averaged energy and displacement of the inverted flag both increase with an increase in the flow velocity, revealing that the amplitude of the inverted flag gives a good estimate of the strain energy. However, the conversion ratio R first increases before reaching a maximum just after the critical velocity and finally decreases with a successive increase in the flow velocity.

The linear analysis of the inverted flag shows that $k = 1.875$ gives reasonably good agreement with the critical flow velocities obtained from the experiments at small mass ratios, with $k = 4.694$ for an isolated conventional flag. However, the discrepancy can reach an order of magnitude for large mass ratios. This is mainly because the viscosity is not considered, and the static divergence instability is not satisfied. When reducing the mass ratio M_S of the flag at large mass ratios, the critical velocity at which the oscillation occurs increases, but the critical velocity at which the oscillation disappears is the same, indicating that the mass ratio has some influence on the critical velocity in the water tunnel experiments.

The theoretical analysis of the two parallel inverted flags shows that the straight mode, the anti-phase flapping mode and the in-phase flapping mode occur with an increase in the flow velocity. The flags in the wind tunnel present the above three modes in turn as the flow velocity increases. The range of the in-phase flapping mode becomes smaller as the separation distance d^* increases. Meanwhile, the disturbance growth rate ratio γ becomes increasingly closer to 1. Under this condition, a multiple flapping state occurs. When $n = 2q$ and $2q + 1$ $(q \geqslant 1)$, 2^q and $2^q + 2^{(q-1)}$ coupled flapping modes will appear, respectively. Additionally, only two of these flapping modes are dominant under most parameters.

The theoretical analysis in this paper is an extension of previous studies (Shelley *et al.* 2005; Jia *et al.* 2007; Schouveiler & Eloy 2009) on the linear theoretical model

of a conventional flag, which fully demonstrates its good applicability. Although the theoretical model has inevitable shortcomings, some intuitive results and quantitative critical velocities can be obtained, indicating its high reliability. In addition, while the theoretical model is indeed nonlinear, the simple calculation process and easy operability give it good application prospects. However, given that the fluid viscosity, the finite length of the flag and leading-edge vortex shedding are not taken into consideration in our linear theoretical model, a more precise theoretical model should be proposed in the future in order to gain a deeper understanding of the nonlinear dynamic behaviour of inverted flags.

Acknowledgements

Declaration of interests

The authors report no conflict of interest.

REFERENCES

ALLEN, J. J. & SMITS, A. J. 2001 Energy harvesting ell. *J. Fluids Struct.* **15**, 629–640.

CHEN, Y. J., YU, Y. L., ZHOU, W. W., PENG, D. & LIU, Y. Z. 2018 Heat transfer enhancement of turbulent channel flow using tandem self-oscillating inverted flags. *Phys. Fluids* **30**, 075108.

FAN, B. 2015 Fluid-structure Interactions of Inverted Leaves and Flags. BS thesis, California Institute of Technology.

GIBBS, S. C., SETHNA, A., WANG, I., TANG, D. & DOWELL, E. H. 2014 Aeroelastic stability of a cantilevered plate in yawed subsonic flow. *J. Fluids Struct.* **49**, 450–462.

GURUGUBELLI, P. S. & JAIMAN, R. K. 2015 Self-induced flapping dynamics of a flexible inverted foil in a uniform flow. *J. Fluid Mech.* **781**, 657–694.

HU, Y. W., WANG, J. S., WANG, J. J. & BREITSAMTER, C. 2019 Flow-structure interaction of an inverted flag in a water tunnel. *Sci. China-Phys. Mech. Astron.* **62** (12), 124711.

HUERTAS-CERDEIRA, C., FAN, B. & GHARIB, M. 2018 Coupled motion of two side-by-side inverted flags. *J. Fluids Struct.* **76**, 527–535.

JIA, L. B., LI, F., YIN, X. Z. & YIN, X. Y. 2007 Coupling modes between two flapping filaments. *J. Fluid Mech.* **581**, 199–220.

JIA, L. B. & YIN, X. Z. 2008 Passive oscillations of two tandem flexible filaments in a flowing soap film. *Phys. Rev. Lett.* **100**, 228104.

JIA, L. B. 2009 The interaction between flexible plates and fluid in two-dimensional flow (in Chinese). PhD thesis, University of Science and Technology of China.

KIM, D., COSSÉ, J., HUERTAS-CERDEIRA, C. & GHARIB, M. 2013 Flapping dynamics of an inverted flag. *J. Fluid Mech.* **736**, R1.

KIM, H. & KIM, D. 2019 Stability and coupled dynamics of three-dimensional dual inverted flags. *J. Fluids Struct.* **84**, 18–35.

KORNECKI, A., DOWELL, E. H. & O'BRIEN, J. 1976 On the aeroelastic instability of two-dimensional panels in uniform incompressible flow. *J. Sound Vib.* **47** (2), 163–178.

ORREGO, S., SHOELE, K., RUAS, A., DORAN, K., CAGGIANO, B., MITTAL, R. & KANG, S. H. 2017 Harvesting ambient wind energy with an inverted piezoelectric flag. *Appl. Energy* **194**, 212–222.

PARK, S. G., KIM, B., CHANG, C. B., RYU, J. & SUNG, H. J. 2016 Enhancement of heat transfer by a self-oscillating inverted flag in a Poiseuille channel flow. *Intl J. Heat Mass Transfer* **96**, 362–370.

RYU, J., PARK, S. G., KIM, B. & SUNG, H. J. 2015 Flapping dynamics of an inverted flag in a uniform flow. *J. Fluids Struct.* **57**, 159–169.

SADER, J. E., COSSÉ, J., KIM, D., FAN, B. & GHARIB, M. 2016 Large-amplitude flapping of an inverted flag in a uniform steady flow-a vortex-induced vibration. *J. Fluid Mech.* **793**, 524–555.

SCHOUVEILER, L. & ELOY, C. 2009 Coupled flutter of parallel plates. *Phys. Fluids* **21** (8), 081703.

SHELLEY, M., VANDENBERGHE, N. & ZHANG, J. 2005 Heavy flags undergo spontaneous oscillations in flowing water. *Phys. Rev. Lett.* **94**, 094302.

SHELLEY, M. J. & ZHANG, J. 2011 Flapping and bending bodies interacting with fluid flows. *Annu. Rev. Fluid Mech.* **43**, 449–465.

SHOELE, K. & MITTAL, R. 2016 Energy harvesting by flow-induced flutter in a simple model of an inverted piezoelectric flag. *J. Fluid Mech.* **790**, 582–606.

TANEDA, S. 1968 Waving motion of flags. *J. Phys. Soc. Japan* **24** (2), 392–401.

TANG, C., LIU, N. S. & LU, X. Y. 2015a Dynamics of an inverted flexible plate in a uniform flow. *Phys. Fluids* **27**, 073601.

TANG, D., GIBBS, S. C. & DOWELL, E. H. 2015b Nonlinear aeroelastic analysis with inextensible plate theory including correlation with experiment. *AIAA J.* **53** (5), 1299–1308.

WATANABE, Y., SUZUKI, S., SUGIHARA, M. & SUEOKAM, Y. 2002a An experimental study of paper flutter. *J. Fluids Struct.* **16** (4), 529–542.

WATANABE, Y., ISOGAI, K., SUZUKI, S. & SUGIHARA, M. 2002b A theoretical study of paper flutter. *J. Fluids Struct.* **16** (4), 543–560.

YOUNG, D. & FELGAR, R. P. 1949 *Tables of Characteristic Functions Representing Normal Modes of Vibration of a Beam*. p. 4913. The University of Texas Publication.

YU, Y. L., LIU, Y. Z. & CHEN, Y. J. 2017 Vortex dynamics behind a self-oscillating inverted flag placed in a channel flow: time-resolved particle image velocimetry measurements. *Phys. Fluids* **29**, 125104.

YU, Y. L., LIU, Y. Z. & CHEN, Y. J. 2018 Vortex dynamics and heat transfer behind self-oscillating inverted flags of various lengths in channel flow. *Phys. Fluids* **30**, 045104.

ZHANG, J., CHILDRESS, S., LIBCHABER, A. & SHELLEY, M. 2000 Flexible filaments in a flowing soap film as a model for one-dimensional flags in a two-dimensional wind. *Nature* **408**, 835–839.